RSC Advances

PAPER

View Article Online
View Journal | View Issue

Cite this: *RSC Adv.*, 2025, **15**, 28524

P_4Se_3 IMC: a new frontier in nanoelectronics

Alia Jabeen * and Abdul Majid

This study examines the fundamental electronic, structural and quantum transport properties of a novel inorganic molecular crystal (IMC), considering both the three-dimensional (3D) bulk and two-dimensional (2D) surfaces/slabs with (001) and (110) surface terminations. The structural properties and bonding analysis carried out using electronegativity differences, bond length analysis, and the Pauling formula reveal strong 3D anisotropy in the bonding of the structure, characterized by strong intramolecular bonding in the distinct molecular units and weak Van der Waals (vdW) interactions between them, confirming the IMC nature of the material. These results were also confirmed by interaction studies, *i.e.* periodic energy decomposition analysis (pEDA-NOCV). Electronic structure computation reveals that the bulk and slab-(110) exhibited semiconducting behavior with band gaps of ~1.54 eV and 0.9 eV, respectively. However, the slab-(001) surface termination corresponds to a narrow band gap of ~0.54 eV. Considering this key feature, the potential of slab-(001) as a nano-electronic device was investigated using the non-equilibrium Green's function (NEGF) strategy. Investigation of frontier orbitals, current–voltage (*I*–*V*) characteristics, and transmission spectra shows the promising field-effect transistor (FET) behavior of the slab-(001) indicating its potential for implementation in nano-scale electronic devices.

Received 13th June 2025
Accepted 24th July 2025

DOI: 10.1039/d5ra04194e

rsc.li/rsc-advances

1. Introduction

The increasing demand for functional materials with tailored characteristics at the molecular level has resulted in inorganic molecular crystals (IMCs) being at the forefront in the fields of material science, physics and chemistry.[1–4] In contrast to conventional solid-state periodic materials, IMCs are periodic materials consisting of distinct, well-defined inorganic molecular units connected through comparatively weak forces/interactions such as hydrogen bonds or Van der Waals (vdW) interactions.[5,6] However, due to the absence of H-atoms, vdW interactions are regarded as the primary interactions. Additionally, strong short-range forces are present in each single molecular unit. The presence of these strong short-range forces in the molecular unit and weak long-range forces between the molecular units creates anisotropy in the bonding within a single molecule. This unusual structural feature provides IMCs with a diverse range of properties that act as a bridge between periodic materials and distinct molecules, offering excellent opportunities to design materials with tuned magnetic, electronic, catalytic and optical properties.[7,8]

The intrinsic adaptability of IMCs, as a result of the broad inorganic and organometallic molecular building blocks, enables the preparation of 2D materials with rational designs along with atomic-level precision. The synthesis methods of conventional vdW crystals, such as layered materials, have been well developed to date.[5] Taking advantage of the layered structure, owing to the enormous mechanical anisotropy, 2D conventional layered materials can be synthesized through the mechanical exfoliation strategy, as with the in-plane chemical bonds within the single layers, slender flakes could persist through the exfoliation processes. In contrast to this, 2D-IMCs are not amenable to preparation through the mechanical exfoliation strategy of the respective bulk counterparts due to the isotropic crystal structure. IMC crystals could be cleaved into distinct crystallographic planes owing to their homogeneous nature; however, the exfoliation process typically results in small particles rather than flakes. In addition, the finely-tuned chemical vapor deposition (CVD) technique, used for layered materials, cannot be used for the preparation of 2D-IMCs because of the isotropic nature of the IMC materials. The growth of layered materials by CVD significantly depends on the major thermodynamic difference, which is experienced by the chemical precursors for out-of-plane and in-plane growth. This synthesis method also faces serious challenges, as the synthesis and preparation of the 2D-IMCs are under investigation. The periodic vdW forces within IMCs often result in energetic isotropy within the growth kinetics, resulting in problems in the growth of the respective 2D counterparts. For the synthesis of 2D-IMCs, the disruption of the isotropic growth kinetics is crucial for the out-of-plane as well as the in-plane growth. Thanks to the surface-passivation method, 2D non-layered flakes can grow.[9] Several chemicals, such as Cl and Se, were included in the CVD procedure in order to passivate the surface of the nucleated flakes of Sb_2O_3 in addition to suppressing the

a, Department of Physics, University of Gujrat, Gujrat, Pakistan. E-mail: aliajabeen777@gmail.com

growth mechanism in the out-of-plane direction.[3] Slender flakes of the well-known IMC antimony oxide (Sb_2O_3), were prepared with lateral sizes in the range from a few micrometers. Among these, some flakes with thicknesses down to a single layer (~0.64 nm) were also produced on a mica substrate.[3,5]

In addition to experimental techniques, theoretical studies of vdW solids, such as layered materials and IMCs, face distinct challenges, including the accurate prediction of the material's environment and the incorporation of both short-range strong forces (covalent or ionic bonding) and long-range vdW forces.[10–16] For the accurate prediction of a material's properties, the choice of accurate input parameters is crucial. For example, the use of accurate exchange-correlation functionals is vital to studying a material's prospects. For the inclusion of vdW interactions, various dispersion corrected functionals such as D, D2, D3, and D4 have been developed according to theory. The D3 theory and functional have been proven to have better results compared to the others, and D4 has shown inferior results compared to D2. Hence, the appropriate functional for the inclusion of the vdW interactions is the D3 functional.[17–20]

The intrinsic inherent anisotropy in bonding in IMCs could result in highly direction dependent properties making them potential candidates for several applications with specific dimensionalities in mechanical response, charge transport, optical absorption, *etc.*[21,22] Furthermore, due to their unique structural attributes, IMCs exhibit specific properties, such as the formation of a distinct dangling, free vdW layer, as observed in the well-known IMC Sb_2O_3. This material is considered a high-k dielectric material and finds applications as an extended vdW dielectric material that could support the integration of 2D devices with excellent performance.[5,23,24] Besides this, vdW dielectric materials could be deposited onto 2D channel semiconductors in order to prepare a field-effect transistor (FET). Furthermore, the vdW interface between an IMC and conventional 2D materials is free from trap states as well as dangling bonds. The vdW dielectric surface of Sb_2O_3 has resulted in greater mobility of the charge carrier and greater device switching stability of the MoS_2-based FET. Inorganic molecular units lead to the formation of a dense film, consequently blocking the gate leakage current within the FET. The exceptional dielectric properties of the Sb_2O_3 surface affect the device performance.[23]

The A_4B_3 molecule's structure (where A = As, P; B = Se, S) has been obtained from the tetrahedron A_4 through the insertion of bridging B atoms, *i.e.* chalcogen atoms, into the three bonds of one P or As atom at the corner of the equilateral triangle made by the remaining three As or P atoms.[25] The bond lengths in this molecule are in agreement with the sum of the covalent radii of the atoms and hence, covalent bonding is exhibited. Considering the thermal stability of the material, the stability of the A_4B_3 molecule varies. The tetraphosphorus tri-sulphide P_4S_3 molecule is highly stable, and Raman and infrared studies indicate the preservation of the molecular structure in all gaseous, solid and molten phases. Furthermore, molecular dynamic computation revealed the thermal stability at ~2000 K.[26]

In addition, considering the crystal structure of A_4B_3 type compounds, most crystallize in *Pnma* or *Pnmb* structures, and the atomic packing is similar to hexagonal close packing. However, not all the compounds are of the same type. The structural configuration variation in molecular ordering across symmetric planes, as well as the number of atoms or molecules within the unit cell must be considered. The non-bonding interactions align well with the sum of the vdW radii, exhibiting the lack of stronger covalent interactions in the vicinity of the intermolecular bonds. Tetraphosphorus tri-selenide generally occurs in four crystalline phases: two room temperature crystalline phases, α-P_4Se_3 and α'-P_4Se_3, and two high temperature phases that are highly disordered, β-P_4Se_3 and γ-P_4Se_3.[27,28] Studies unveil unique traits, suggesting intramolecular–intermolecular coupling, as observed in the case of Se atoms.

P_4Se_3 has been explored as a material attracting remarkable interest, specifically because of its recent recognition as an IMC by high-throughput computation as well as machine learning studies.[5,6] The initial studies have explored the intermolecular interactions,[6] transport properties,[29] and prospects of the material in Li-ion,[30] Na-ion batteries,[31] and then multivalent ion batteries.[32] Furthermore, adding a magnetic element, *e.g.*, iron (Fe), would induce hard ferromagnetism in the materials.[33] All of these studies have been conducted at the molecular level and most of them by using DFT-based codes. However, there is still a lack of detailed studies on periodic materials, the discovery of the nature of the periodic form, and finding their potential to be used in appropriate applications in their periodic form. Though extensive research is available on typical 2D materials,[5] detailed studies of novel IMCs for various functionalities, including S_8, As_2O_3, SbI_3, *etc.* that have been suggested as IMCs, are still lacking. This study addresses this critical gap by rigorously suggesting P_4Se_3 as a novel IMC and presenting a comprehensive theoretical study of the fundamental electronic and structural properties alongside transport properties in its bulk and surface, where for the surface the (001) and (110) planes were considered and indicated by slab-(001) and slab-(110), respectively. The results, as obtained by DFT-based codes, *i.e.*, VASP and non-equilibrium Green's function (NEGF) in ADF, shows that the surface termination (001) of P_4Se_3 showed the potential for FET, in an exploration of the landscape of materials for next-generation nano-scale electronics.

2. Computational details

Structural relaxation and electronic property computation were performed for the bulk and slabs by utilizing density functional theory (DFT) as executed in the Vienna *Ab initio* Simulation Package (VASP).[34–37] The generalized gradient approximation (GGA) with Perdew–Burke–Ernzerhof (PBE)[38–40] was implemented for the exchange-correlation energy. For the accurate consideration of the weak vdW interactions between the molecular units, Grimme's D3 correction along with the Becke–Johnson damping (DFT-D3-BJ) was considered.[17]

The electronic-ionic interactions were expressed by utilizing the projector augmented wave[41] method with a plane wave cutoff value of 650 eV. The reciprocal space or Brillouin-zone

integration for the structural and electronic structure computation was executed utilizing the mesh size of 5 × 4 × 3 for a Monkhorst–Pack mesh. However, for the optimization of the slabs/surfaces, the *K*-point mesh of 5 × 4 × 1 with a vacuum of 20 Å was given along the *z*-axis in order to minimize the mock interactions between periodic layers. The specific *K*-point mesh was chosen after performing a convergence test, and minimum energy *K*-points were taken into consideration. Convergence tests were carried out to ensure the appropriateness of the *K*-points, cut-off values and functional.

The cubic crystal structure was considered as the initial geometry, with lattice parameters $a = 10.606$ Å, $b = 11.891$ Å, $c = 14.950$ Å and $\alpha = \beta = \gamma = 90°$, as shown in Fig. 1. The reason to choose this specific crystal structure was that it consists of the inorganic molecular units of P_4Se_3 that are separated by a specific distance indicating a high probability of the material existing as an IMC.[3,5] The surfaces/slabs were made along the specified planes, *i.e.* (001) and (110), and termed as slab-(001) and slab-(110) respectively. The VESTA software was used to generate the above described structures. Structural optimization was carried out until the forces applied on each atom were less than 1×10^{-6} eV Å^{-1}, and the total energy change between the adjacent iterations was smaller than 1×10^{-8} eV. Interaction studies were carried out using periodic decomposition analysis (pEDA-NOCV) on the bulk and surface structure, for which only two fragments were taken into account and each fragment was the molecular unit consisting of the P_4Se_3.[7] The density of states (DOS) and band structure of the relaxed geometries were determined using VASP. The values of the band gap were estimated by using the DOS and electronic band structure.

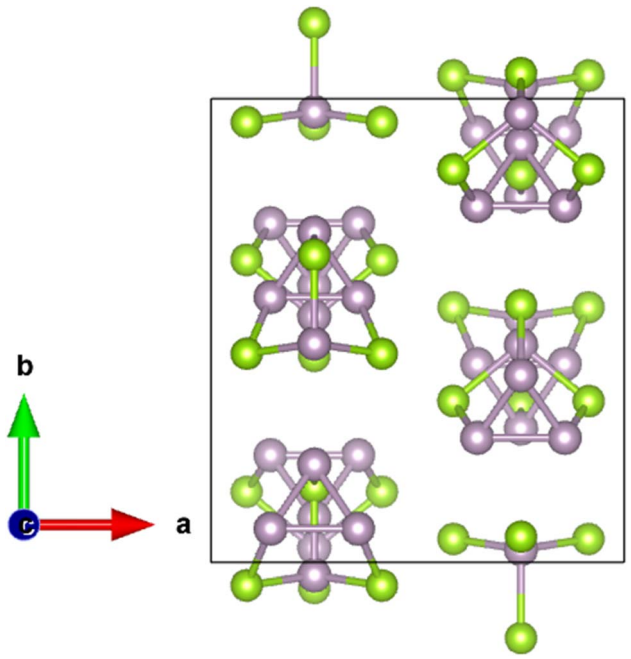

Fig. 1 The initial geometry of the cubic crystal structure of P_4Se_3, where the green and purple colored balls represent the Se and P atoms, respectively.

The quantum transport characteristics of the P_4Se_3 of slab-(001) were computed, involving the transmission spectra, current–voltage (*I–V*) curves and frontier orbitals, in order to check the possibility of the material being used as a nano-device. These transport properties were computed using the density functional tight binding (DFTB) formalism as implemented in Amsterdam Density Functional (ADF) code. The two probe system was made up of gold (Au) leads as the right and left electrode and slab-(001) P_4Se_3 as the central region or scattering region. Au-slabs were used as the leads with the 2 × 2 × 1 supercell of Au.

The non-equilibrium Green's function (NEGF) methodology was used in order to compute the quantum transport properties as implemented in ADF code. The TZP basis set and the D3-BJ functional were used for these calculations, in conjunction with the GFN1 xTB model. A "very good" accuracy setting was employed to ensure reliable results. The transmission spectra and *I–V* profile were calculated by applying the bias voltage across the Au-leads, and graphs were obtained. The impact of the gate voltages on the transport characteristics was computed. The frontier orbitals were also visualized by utilizing the in-built tools in the ADF-code.

3. Results and discussion

3.1. Structural properties

3.1.1. Bulk. The optimized structure of P_4Se_3 in bulk periodicity is illustrated in Fig. 2. The optimized structure revealed that the material consists of molecular cages/units that are settled at a specific distance from each other. The molecular cage is made up of a P_4Se_3 molecule, as can be seen in the Fig. 2, where the green and purple balls represent selenium (Se) and phosphorus (P) atoms. Furthermore, it can be seen that each Se and P atom is involved in two and three bonds, respectively, as per the respective valence shell configuration, *i.e.* 2 for Se atoms and 3 for P atoms.

The optimized lattice parameters for the bulk P_4Se_3 material are as follows: $a = 6.128$ Å, $b = 7.813$ Å and $c = 6.652$ Å, and the optimized volume of the unit-cell under consideration (56 atoms) is 300.824 Å^3.

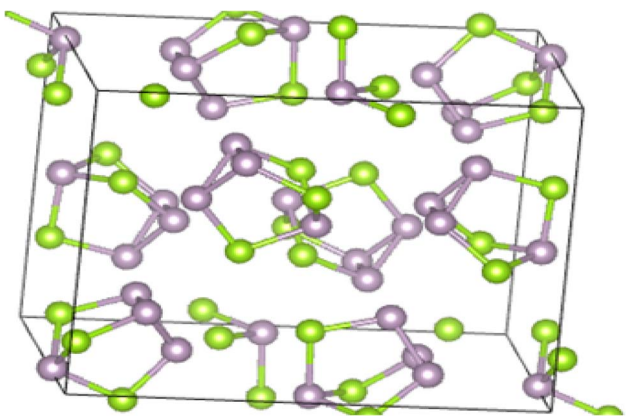

Fig. 2 Optimized crystal structure of bulk P_4Se_3, where green and purple balls represent the Se and P atoms, respectively.

The bonding of the material can be discussed on the basis of the electronegativity difference of the elements present in the material. The electronegativities of P and O are 2.19 and 2.55, respectively. The electronegativity difference in P_4Se_3 is 0.36, which indicates the presence of strong covalent bonding, *i.e.* short-range forces.[7,17] Furthermore, the ionic character of the material can be determined using Pauling's formula, indicating the percentage ionic character to be 10.58%.

Additionally, bond length analysis can be performed for the optimized structure. The P–Se bond length is 2.70 Å, whereas the P–P bond length is 2.48 Å. Both of these are considered when considering atoms in adjacent molecular units/cages, which means this is the intermolecular distance. The bond distance shows the presence of long range forces, *i.e.* weaker vdW forces, as the bond distance is greater than 2.4 Å. In contrast, the intra-molecular distances, *i.e.* Se–P = 2.26 Å, P–P = 2.24 Å, evidence the presence of short-range forces due to the presence of relatively small bond distances, hence there exist strong forces, which can be summarized as the primary type of bonding. The presence of weak forces in the vicinity of the inter-molecular region and stronger forces in the intra-molecular region showed that there exists anisotropy in bonding throughout the structure *i.e.* 3D anisotropy.

3.1.2. Surfaces. After the bulk structure optimization, the bulk was sliced to form surfaces at specific orientations, *i.e.* (001) and (110), regarded as slab-(001) and slab-(110), respectively.

3.1.2.1. Slab-(001). The optimized structure for slab-(001) of P_4Se_3 is presented in Fig. 3, where the green and blue balls show the Se and P atoms, respectively. The optimized lattice constants were $a = 9.635$ Å; $b = 10.710$ Å; $c = 33.555$ Å and $\alpha = 90°$; $\beta = 90°$; $\gamma = 90°$. Furthermore, the bond intra-molecular and inter-molecular distances of the relaxed structure were computed, and were 1.66–2.26 Å and 3.9 Å, respectively.[32] The bond distances unveiled the presence of the strong forces within the cages, whereas the weak vdW forces are present between the cages as the bond distance is greater than 2.4 Å (benchmark). The bonding of the material can also be discussed based on the bond distances and respective radii (covalent, ionic and vdW) of the respective elements present in the materials. A bond is considered strongly covalent if the sum of the covalent radii is smaller than the calculated bond distance, or if the sum of the ionic radii is larger than the bond distance between the atoms. For the P_4Se_3 material, the sum of the covalent radii of P and Se is 2.26 Å (P = 1.06 Å, Se = 1.20 Å), whereas the sum of the ionic radii is 2.15 Å (P = 1.00 Å, Se = 1.15 Å). Comparison with the intra-molecular distances unveiled the presence of stronger covalent bonds in the vicinity of every single molecular cage, *i.e.*, in the intra-molecular region. Moreover, the vdW radii for P_4Se_3 show that the material exhibits vdW interactions between the molecular cages, *i.e.*, in the vicinity of the inter-molecular region, as the vdW radii were 3.7 Å (P = 1.80 Å, Se = 1.90 Å). From the above discussion, it can be concluded that there is 3D anisotropy in the bonding within the single crystal structure of P_4Se_3.

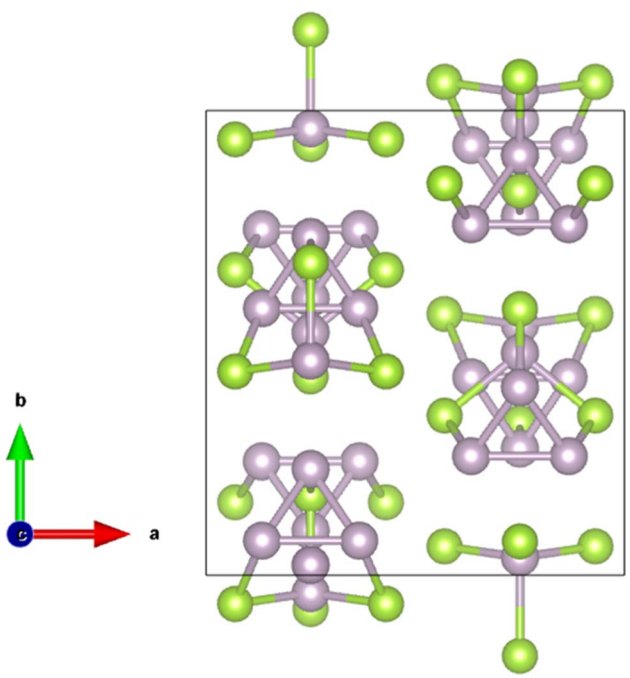

Fig. 3 The optimized structure for slab-(001) of P_4Se_3.

3.1.2.2. Slab-(110). Similar to previous cases, the slab-(110) of P_4Se_3 was optimized, and the optimized structure is provided in Fig. 4. Each molecular unit consists of a P_4Se_3 molecule, and the units are separated from each other as described previously. The optimized lattice constants are $a = 13.644$ Å, $b = 13.644$ Å, $\alpha = 96.41°$, $\beta = 96.41°$, and $\gamma = 76.54°$. The optimized intra-molecular bond distance was P–Se = 2.25 Å, whereas the intermolecular bond distance was P–Se = 3.54 Å, revealing the intramolecular strong bonding and intermolecular weak bonding.

3.2. Interaction studies

Although the interactions within and between the molecular units in the IMC have been theoretically discussed based on electronegativity differences, Pauling's formula, and bond length analysis, a complete study is presented here to discuss these interactions in the IMC in greater detail. Periodic energy decomposition analysis with natural orbitals for chemical valency (pEDA-NOCV) was performed. The pEDA-NOCV is based on the fragments, between which the interactions are studied, and hence it is highly effective to study the intermolecular and intramolecular interactions. Here, only two molecular units of P_4Se_3 were considered, where each molecular unit was an independent fragment. The arrangements are as shown in Fig. 5.

3.2.1. Bulk. The pEDA analysis, in general, results in various energy terms, *i.e.* interaction energy terms, which are the main energy terms, steric interactions dealing with the hindrance created by the valence and core elements and orbital energy.[7] The interaction energy is the sum of the Pauli energy, dispersion energy, electrostatic energy and orbital energy. The Pauli energy term is an indication of the repulsive interaction stemming from the Pauli exclusion principle that impedes

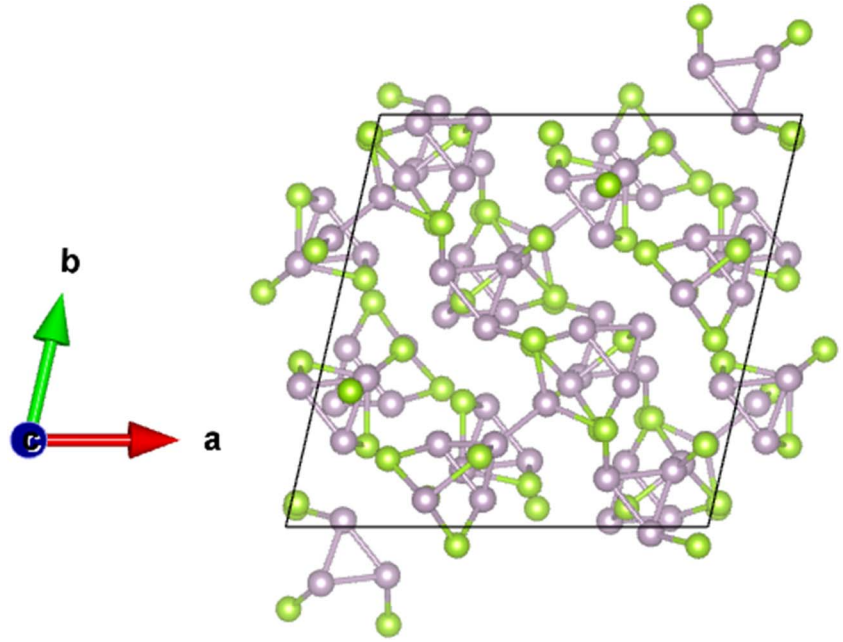

Fig. 4 The optimized structure of slab-(110) of P_4Se_3.

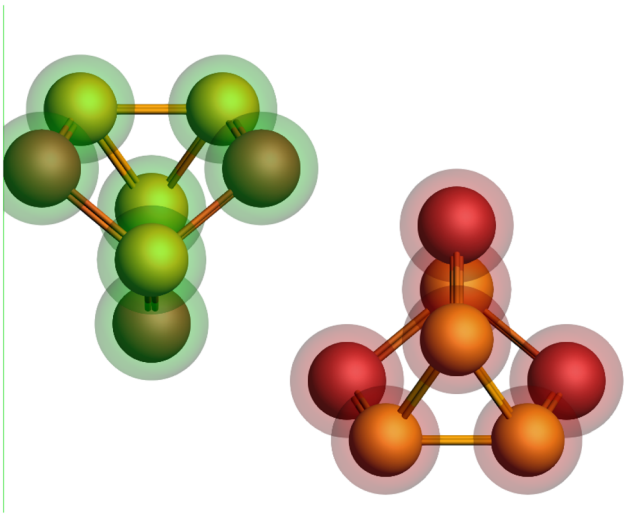

Fig. 5 The arrangement of fragments of P_4Se_3 in the pEDA-NOCV analysis.

electrons of the same spin occupying the same orbital or a similar region of space. This is the steric repulsion as the two electronic clouds overlap.[42–44] The value of the Pauli energy is 1.27 eV, which represents repulsive interactions. The dispersion energy term represents attractive London dispersion interactions that stem from the instantaneous dipoles in the electronic component and hence is of prime importance for non-covalent forces, specifically vdW interactions. The value of the dispersion energy is −0.68 eV, showing the attractive contribution of the energy. The electrostatic term represents the classical electrostatic interactions between the two fragments, based on their unperturbed charge distributions. It adds to the interactions between the permanent dipoles and multipoles. The computed value of the electrostatic interactions are −0.66 eV, indicating attractive electrostatic interactions. In addition, the orbital energy term captures the lowering of the energy because of the mixing of occupied orbitals from one fragment with the other fragment's unoccupied orbitals. Additionally, the mixing of the occupied orbitals of one fragment with the occupied orbitals of the other fragment is also considered. This term is important for the inclusion of the covalent bonding along with the contribution of non-covalent interactions. Furthermore, the orbital energy, which constitutes the main bond energy terms, is further decomposed into the kinetic energy, electrostatic energy and exchange–correlation energy components. The computed kinetic energy value is large, *i.e.* ∼−14.56 eV, indicating the conventional stronger primary interactions, *i.e.* covalent bonding, and then the energy is decreased as the bond is formed. The electrostatic energy variation accompanied by the orbital mixing is computed in the form of the electrostatic energy, and its value is large and positive *i.e.*, ∼12.46 eV, indicating that the electrostatic contribution within the orbital interactions is repulsive. This is a usual attribute of the EDA, as estimation of the charge densities in the process of mixing of orbitals could take some of the repulsions from the electrostatic part that is overcome through lowering of the K. E. Similarly, the exchange correlation energy related to the mixing of the orbitals is also computed, and its value is 16.20 eV, indicating the repulsive contribution in the overall orbital energy term. The overall orbital energy, as discussed above, is −0.47 eV, indicating the attractive interactions over the orbital mixing. The orbital energy is attractive in nature with a value of −0.47 eV. The interaction energy term is the sum of the Pauli energy, orbital energy, electrostatic energy and dispersion energy and explains the overall interactions or strength of bonding between

the two fragments. The computed value of the interaction energy was −0.55 eV, showing that the interactions between the fragments were energetically favorable. Furthermore, the results indicate that the attractive and repulsive terms are balanced, and overall, the attractive part dominates the total interaction energy term. Conclusively, the attractive terms dominate between the two molecular units, indicating the presence of intermolecular interactions. However, their small magnitude reveals that these forces are weak. Furthermore, the dominance of the attractive term is responsible for keeping the molecular units intact within the material.[7,17,45,46]

Additionally, the pEDA-NOCV orbitals were also drawn (not given here), and the results indicated the localization of orbitals on the molecular units and the absence of any electronic cloud in the vicinity of the intermolecular region. This indicates the presence of strong covalent bonding in the molecular region, yet the weak interactions are present in the inter-molecular region as evident from the energy terms.

3.2.2. Slab. Similar to the previous case, the pEDA analysis was performed for the surface system. The overall interaction energy was −0.54 eV, indicating the net attractive interactions along with the energetic feasibility of the formation of the material. The interaction energy was the sum of the respective energy terms from the Pauli energy (1.27 eV), dispersion energy (−0.67 eV), electrostatic energy (−0.66 eV) and orbital energy (−0.47 eV). The notable negative/attractive contributions from the electrostatic, dispersion and orbital energy terms are effectively balanced by the positive/repulsive Pauli exclusion terms.

The orbital energy term (−0.02 eV) is the sum of the K. E. (−0.52 eV), electrostatic energy (0.44 eV) and exchange correlation energy term (0.06 eV). The attractive term dominates in the orbital interactions, which is because of the large K. E. values and is balanced by the repulsive exchange correlation and electrostatic energy.

Furthermore, the pEDA-NOCV orbitals were also drawn, indicating the presence of an electronic cloud in the region of the molecular unit and the absence of the electronic cloud in the inter-molecular region. The results successfully highlight the strong covalent bonding and weak vdW interactions in the intramolecular and intermolecular region, as supported by the previous results.

3.3. Stability analysis

3.3.1. Formation energy analysis. The structural stability of the materials can be discussed based on the formation energy (eV) and formation energy per atom (eV per atom). The formation energy of the materials can be calculated from the difference between the product and the reactant energies. The formation energy was computed for various exchange correlation functionals, as shown in Table 1. The results revealed a negative formation energy, which shows that the material's structure is stable. Furthermore, the minimum energy was computed for GGA-PBE-D3-BJ, indicating the most favorable functional for this case and also corresponding to the literature.[7,17,19,20] This functional *i.e.* GGA-PBE-D3-BJ was used throughout this work.

Table 1 The formation energy analysis of bulk P_4Se_3

Functional	Energy (eV)	Energy/atom (eV per atom)
GGA-PBE-D3	−268.53	−4.80
GGA-PBE-D3-BJ	−274.87	−4.91
GGA-PBE-D4	−260.15	−4.65

The computed values of the formation energy were −4.78 eV per atom and −4.76 eV per atom for slab-(110) and slab-(001), respectively. The negative value indicates the exothermic formation process, and hence, the formation of the respective surfaces is stable. Comparing bulk, slab-(001) and slab-(110), the minimum energy was observed for bulk, and hence, it is the most stable structure. Furthermore, based on the formation energy, the stabilities of the structures can be categorized as bulk > slab-(110) > slab-(001), as the formation energy trend is bulk < slab-(110) < slab-(001).

3.3.2. Phonon analysis. The dynamic stability of the material can be discussed based on a phonon band diagram dealing with the atomic vibrations. The phonon band structure was plotted by taking the *K*-path and frequency along the *x*- and *y*-axes, respectively. The total number of branches depends upon the number of atoms present in the structure according to a relationship, *i.e.* no. of branches = $3N$, where N is the total number of atoms. In this case, the cell of 56 atoms was taken into consideration, and hence the total number of branches would be 168,[7] as shown in Fig. 6 and Table 1 in the SI. The presence of all the positive phonon branches refers to the dynamic stability of the material.[3,47–49]

Furthermore, two major types of branches are present: low-frequency acoustic branches and high-frequency optical branches. The acoustic and optical branches can be differentiated by the following rule: for optical branches, $\omega \rightarrow$ (non-zero constant), as $k \rightarrow 0$, while for acoustic branches, $\omega \rightarrow$ (zero constant), as $k \rightarrow 0$. In summary, for a 0 value of K, ω (frequency) would be non-zero and zero for optical and acoustic branches, respectively, which means that the acoustic branches emerge from zero, whereas the optical branch emerges anywhere except zero. Various phonon modes with the respective frequencies are provided in Table 1 in the SI.

Furthermore, the acoustic branches arise due to the atoms having high atomic mass, *i.e.* Se in this case, whereas the optical branches appeared due to the atoms having smaller atomic masses, *i.e.* P atoms. The frequency gap within the phonon band diagram is assigned to the difference in atomic mass between the elements present in the structure in such a way that when there is more of a mass difference, there would be more of a frequency gap, and *vice versa*.[50–52] Therefore, the frequency gap between the optical and acoustic branches, as can be seen in the phonon band diagram, is due to the major mass difference between the P and Se.[53]

3.4. Electronic properties

The electronic properties of the novel IMCs, *i.e.*, P_4Se_3 in bulk, and its respective surfaces as discussed according to the band

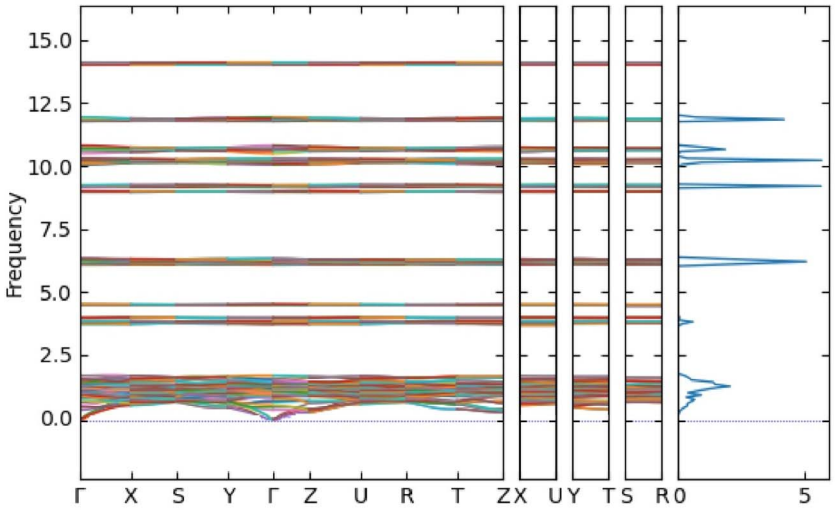

Fig. 6 The phonon spectra for bulk P_4Se_3.

structure and density of states (DOS) are as provided in the following description.

3.4.1. Bulk. The band structure as computed for the bulk P_4Se_3 is provided in Fig. 7, where the Fermi level was set at 0 eV, represented by the blue dotted line. The results showed that the material is an indirect band gap material as both conduction band minima (CBM) and the valence band minima (VBM) occur at different *K*-points. For this material, the movement of charge carriers from the valence band to conduction band releases a phonon in addition to a photon. Furthermore, the band gap of the material was calculated to be 1.54 eV, suggesting its potential suitability for various semiconducting applications, particularly in photocatalysis, *e.g.* photocatalytic water splitting.

For further detailed analysis, the total and partial DOS were computed to describe the contributions arising from the specific orbitals. The DOS for the bulk P_4Se_3 was computed and given in Fig. 8, where the Fermi level was set at 0 eV, as shown by the blue dotted line. The results revealed that the major contribution to the electronic structure arises from the Se atoms, which may be attributed to the higher electronegative value of Se atoms. Furthermore, a considerable contribution arises from the P atoms in the conduction band. In the conduction band, the Se-p_z states overlap with the Se-p_y states, resulting in the formation of π-bonds. Furthermore, the P-s states overlap with the P-p_z states, and the P-p_y states overlap with the P-p_x states, resulting in the formation of the σ-bond.

Similar to above, in the valence band, significant overlap of Se and P atoms can be seen with a major contribution from Se-p_x. In general, the overlap of sub-orbitals of the P and Se atoms can be viewed in the valence band.

In general, the shapes of the curves in the DOS are very important and mostly attributed to the accuracy of the calculations. However, there are several factors affecting the shape, and one of them is the periodicity and binding between the atoms present in the structure. The sharpness of peaks here can be attributed to the vdW forces present between the molecular units. Hence, the weaker vdW forces present between the crystal structure have a strong impact on the electronic structure of the overall materials.

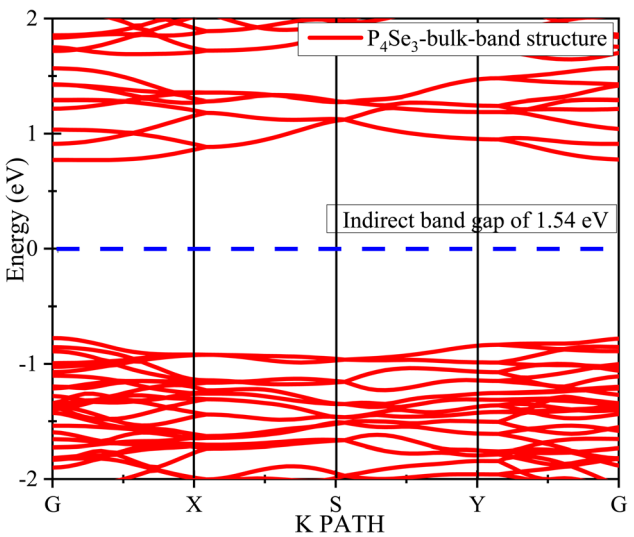

Fig. 7 The electronic band diagram for bulk P_4Se_3, where the Fermi level was set at 0 eV.

3.4.2. Slab-(001). The electronic band structure for the slab-(001) of P_4Se_3 was computed and presented in Fig. 9. The results revealed that the material is a direct band gap semiconductor, as the CBM and VBM exist at the Y *K*-point. Furthermore, the slab-(001) exhibits a band gap of 0.57 eV.

Further detailed analysis of the total and partial density of states, as given in Fig. 10, revealed that the VB mainly consists of Se atoms, whereas the CB has a considerable contribution from the P atoms.

3.4.3. Slab-(110). The electronic partial and total density of states of slab-(110) P_4Se_3, as in Fig. 11, reveals the semiconductor nature of the material. The material exhibits a band gap of ~0.9 eV with a major contribution of Se atoms in both the

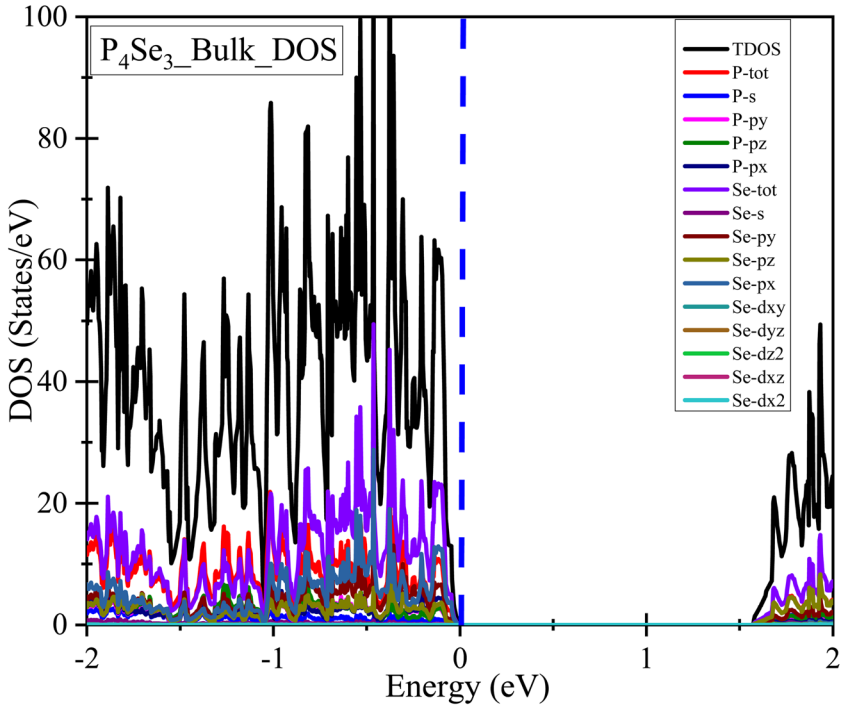

Fig. 8 The total and partial DOS for bulk P_4Se_3, where the Fermi level was set at 0 eV.

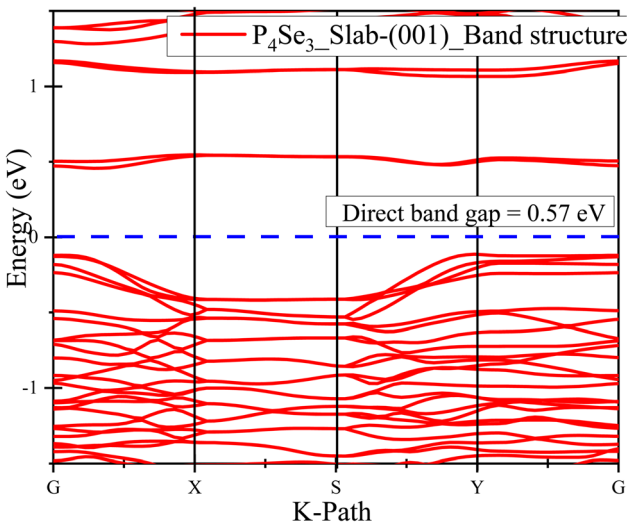

Fig. 9 The electronic band diagram for the slab-(001) of P_4Se_3, where the Fermi level was set at 0 eV, as shown by the blue dotted line.

CB and VB that can be attributed to the high electronegativity of the elements.

It is also important to keep in mind that various GGA functionals, *e.g.*, PBE, are notorious for underestimating band gaps, because of their in-built problems in describing the electronic exchange and correlation effects. Recently, modern theoretical approaches like self-interaction-corrected DFT methodology or hybrid functionals, for example, Heyd–Scuseria–Ernzerhof (HSE03 or HSE06), have shown better accuracy regarding the prediction of band gaps of materials.[54,55] This improved accuracy in predictions of band gaps is achieved by considering the exact part of the exchange or by improving the forged self-interactions. Though the above-described methods provide improved precision, the much greater computational cost could be the limiting factor for the large-scale simulation or screening of materials. For this study, PBE results in a suitable balance between the accuracy and computational cost in order to explore the trends in the basic electronic structure.

3.5. Evaluation of the potential for nano-devices

Because of the low band gap, the material might have potential to be utilized in nano-devices. To investigate the potential, the transport characteristics could be studied. Here, the slab-(001) of P_4Se_3 was investigated as the central part of the nano-device because of its smaller band gap. For the computation of the transport characteristics, the NEGF strategy was adopted,[56,57] for which gold (Au) leads were used as right and left electrodes with slab-(001) acting as the central region, as shown in Fig. 12, where the yellow-colored balls represent the Au atoms and the central region is slab-(001) of P_4Se_3. The transport characteristics were calculated at various applied gate voltages.[58–60]

3.5.1. Frontier orbitals. The frontier orbitals, *i.e.*, highest occupied molecular orbitals (HOMO, HOMO-1) and lowest unoccupied molecular orbitals (LUMO, LUMO+1), provide valuable information and are provided in Fig. 13. The HOMO was spread out in the upper region of the slabs and into the Au-leads/electrodes. The stronger overlap of the HOMO with the electrode suggests better coupling of the orbital with the contact's Fermi level, indicating effective contribution towards the hole transport. The color distribution (blue and red) shows

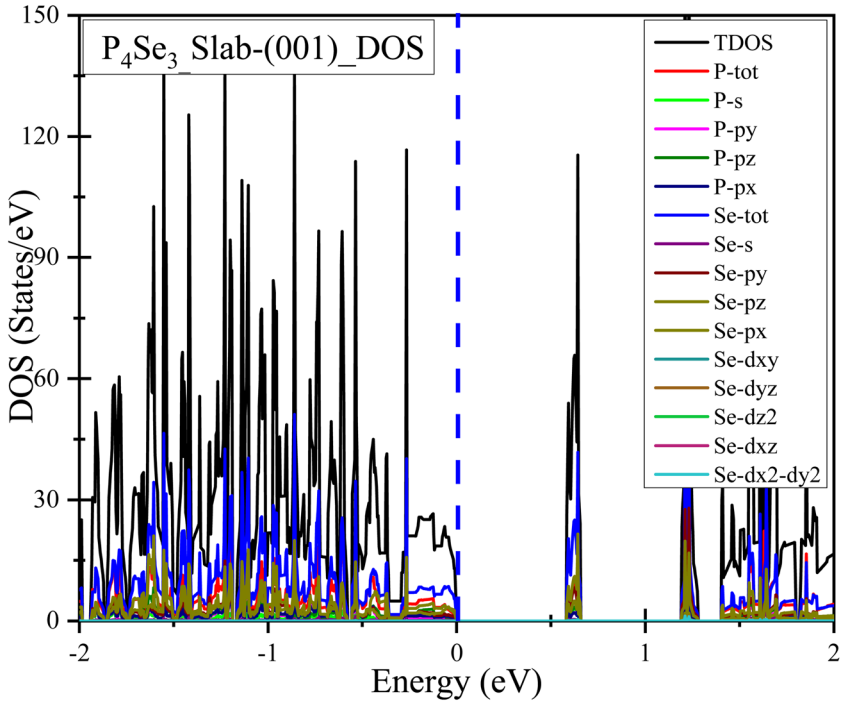

Fig. 10 The electronic partial and total DOS for slab-(001) of P_4Se_3.

the phase of the respective wave function. Akin to the HOMO, in the HOMO−1, the spatial distribution along with the coupling with the electrode was observed. The well-coupled HOMO−1 level shows the contribution to the transport characteristics, specifically in the level occurring in the bias window.

The LUMO, another orbital important for electronic transport, was taken into account by considering the spatial distribution of the central region, *i.e.* slab-(001). The strong coupling of the LUMO with the leads indicates the effective injection along with the electron extraction into the orbital. Furthermore, the spatial pattern as well as the phase distribution are important parameters to be considered. The LUMO+1 orbitals with accessibility to the applied bias could offer another route to electronic transport. Furthermore, the difference in the

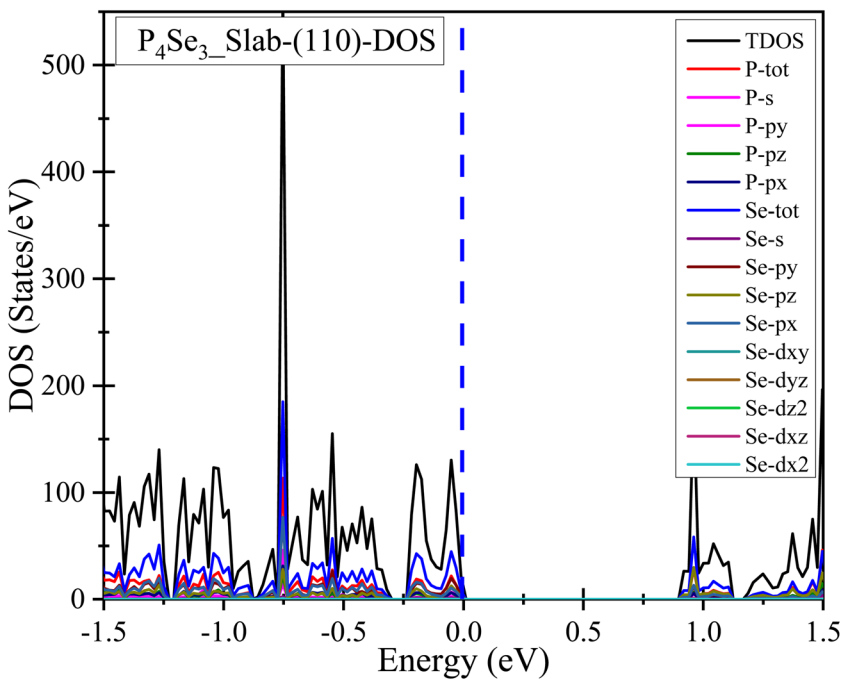

Fig. 11 The electronic partial and total DOS for slab-(110) of P_4Se_3.

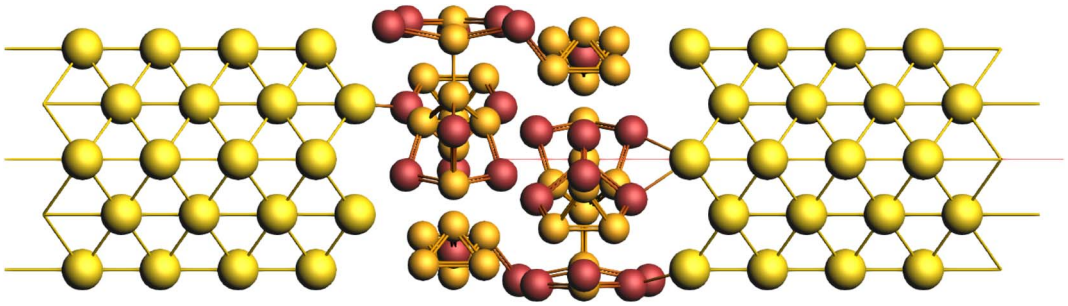

Fig. 12 The arrangement for the NEGF for slab-(001) of P_4Se_3.

spatial pattern compared to the LUMO orbital could be a result of the distinct transport properties.

The appearance of several frontier orbitals, *i.e.* HOMO, LUMO, HOMO−1, and LUMO+1, which are well-coupled with the electrodes, indicated the presence of several transport channels available, based on the applied voltage, along with the alignment of such energy levels with the Fermi levels of the contact. Furthermore, the spatial distribution as well as the specified shapes of such orbitals are influenced by the bonding as well as the atomic structure. However, any modification in the molecular geometry or the presence of defects could considerably change the orbitals and impact the transport characteristics.

3.5.2. Current–voltage (*I–V*) profile. The current–voltage (*I–V*) profiles for slab-(001) of P_4Se_3 were plotted as shown in Fig. 14, and are distinctly non-linear, showing that the device is not like a normal resistor, indicating the presence of barriers, resonant tunneling, or any other complex transport mechanisms in the material. Furthermore, symmetric current behavior for both negative and positive bias voltages was observed at 0 V gate voltage, indicating identical electronic transport characteristics along both directions of the flow of the current.[59,61]

The black curve (IV profile at 0 V) indicates comparatively smaller bias voltages in addition to the non-linear increase in current with the increase in the bias voltages. There may be a slight gap in the transport or the low conductance region close to the 0 V bias. By increasing the gate voltages in the range of 0.5–2 V, the current at the provided bias voltage generally increases compared to the 0 V case. The shape of the curves also changes, indicating the shift in the prevailing transport mechanisms, or in summary, the increase in the concentration of carriers in the channel. Further increase in the gate voltage, *i.e.* 2.5–5 V, leads to significant changes such as increased currents showing that the applied gate voltage improves the conductivity of the material, *i.e.* slab-(001) of P_4Se_3. Furthermore, plateau-like or stepped features can be observed, and may be an indication of several interesting phenomena such as coulomb

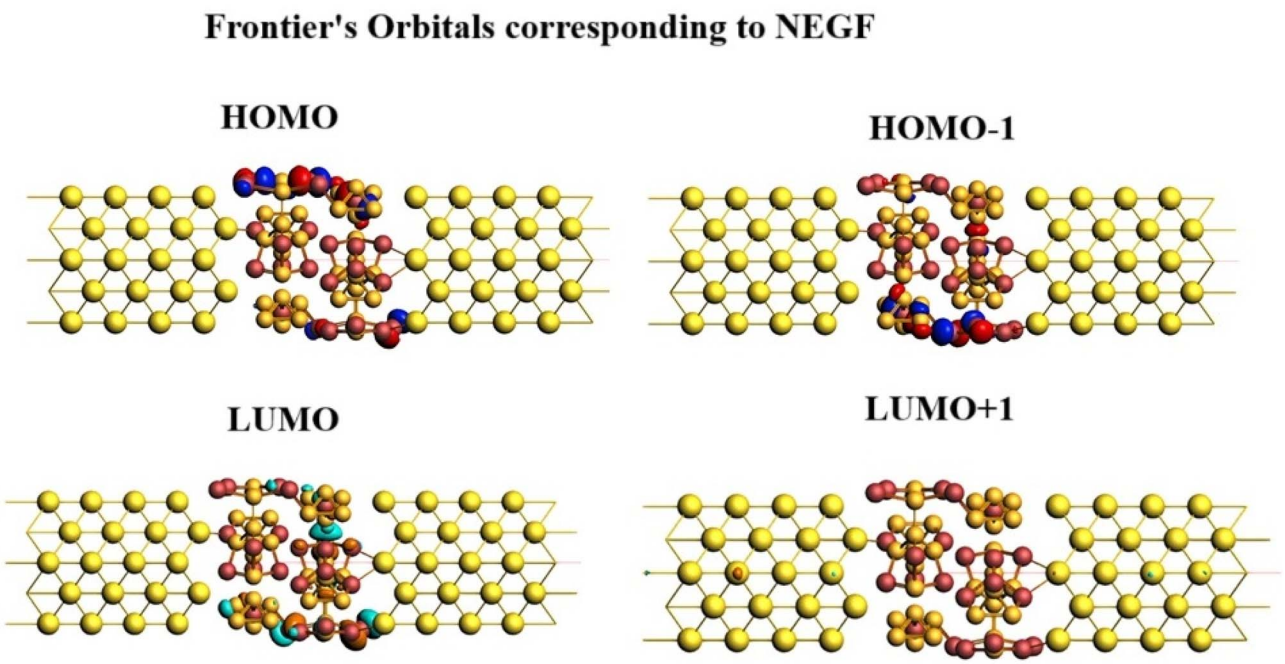

Fig. 13 The frontier orbitals as generated during the NEGF study for slab-(001) of P_4Se_3.

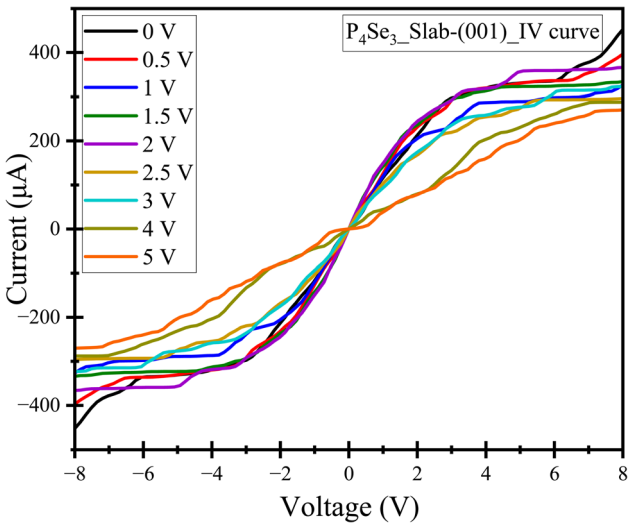

Fig. 14 The current voltage profile for slab-(001) of P_4Se_3 at 0–5 V.

blockade impacts, opening of the brand new transport channels or resonant tunneling by the discrete energy levels. In addition to these effects, asymmetric behavior was observed at amplified/high gate voltages, indicating the fact that the applied gate voltages break the electronic structure symmetry and modify the transport characteristics.

Conclusively, by increasing the gate voltage from 0 to 5 V, a significant shift as well as a change in the shape of the *I–V* curves was observed, indicating the large variation in the transport characteristics of the device under the applied gate voltage. This behavior is trademark behavior similar to field-effect transistors (FETs).

3.5.3. Transmission spectra. To further explore the transport properties, the transmission spectra were computed at the applied voltages, *i.e.*, 0–5 V, and some representative transmission spectra are shown in Fig. 15. The results revealed complex transmission spectra with several dips and peaks as a function of the energy. This shows that the electron transmission probability of the slab-(001) is highly dependent on the energy and affected by the complex electronic structure of the device.[62]

In the absence of the applied gate voltage, *i.e.*, at 0 V gate voltage, a region of low transmission occurs around the Fermi level, which results in a smaller conductance region close to the Fermi level within the *I–V* curve at 0 V. Furthermore, various transmission peaks were present at both negative as well as positive energies, indicating the fact that transport could occur as the injected electron energy aligned with the resonant levels. In contrast, the transmission spectra are modified at 1 V applied gate voltage, as some peaks shifted towards more positive values. However, at the Fermi level, lower transmission occurs, but the values increase to some extent compared to those at 0 V, showing the promising contribution towards the greater current observation in the *I–V* characteristics at 1 V applied gate voltage. Similarly, at 2 V applied gate voltages, a change in the transmission spectra was seen, and the peaks may involve a change in the intensity of already existing peaks. However, at a high gate voltage, *i.e.*, 5 V, the spectra were quite different. The pronounced increase in the transmission probability over a broad energy range was consistent with the amplified *I–V* curve at the applied gate voltage. In general, the appearance of multiple sharp peaks may be attributed to the plateau-like features as observed in the *I–V* curves at the respective applied gate voltages. As the applied bias voltage lines up with the

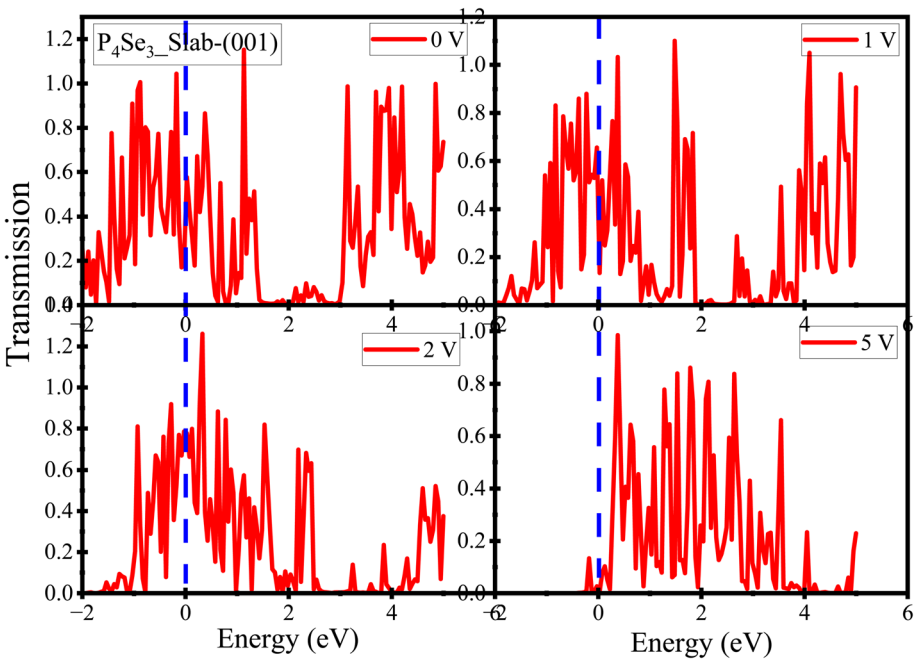

Fig. 15 The transmission spectra for slab-(001) of P_4Se_3 in the range 0–5 V.

electrochemical potentials of the contacts, the energy window encompasses such peaks in the transmission spectra, increasing the current.

Furthermore, transmission gaps at distinct energies can be observed, where the transmission is almost zero, representing the effective blockage through the device. The locations as well as the widths of such gaps seem to be affected by the applied gate voltage. Furthermore, the sharp peaks within the transmission spectra correspond to resonant tunneling at specific energy levels in the devices. At these energies, the electrons have a greater probability of transmission from one contact to another.

3.5.4. Correlation of transmission spectra with *I–V* curves. The lower transmission at 0 eV for the spectra exhibiting the lower conductance at zero bias voltages is consistent with the *I–V* curves. Furthermore, the general increase in the transmission probability as well as the occurrence of the enhanced transmission peaks/pathways at the amplified applied gate voltages correspond to enhanced current levels within the *I–V* profiles. The applied gate voltages improve the electronic structure with the opening of brand new channels for the transport of electrons. The features similar to the plateaus or steps within the *I–V* curves at the greater values for the applied gate voltages (*e.g.* 5 V) can be a direct result of the appearance of the sharp peaks within the transmission spectra. By increasing the bias voltages, the energy window for the transport broadens. The alignment of this window with the sharp transmission resonance leads to the rapid increase in the current, consequently producing a step. The step may exist as the transmission is high over a certain energy range in the bias window.

4. Summary

This paper considers P_4Se_3 as an IMC, and theoretical studies using DFT-based VASP and ADF codes were used to study the fundamental structural, electronic and transport properties of the material. The structural attributes of the material for the bulk and surfaces reveal that the material exists in the form of molecular units that are connected by weak vdW forces. This specific attribute creates 3D anisotropy in the bonding, yet because of the periodic anisotropy the material can be regarded as exhibiting an isotropic nature under the periodic boundary condition. Bonding analysis as performed using theoretical knowledge, *i.e.*, electronegativity difference, bond length analysis, and Pauling's formula, confirmed the fact that the material is anisotropic in terms of its bonding, *i.e.*, it exhibits strong covalent bonding in the molecular units and weak vdW interactions in the inter-molecular region. Furthermore, pEDA-NOCV analysis based on the decomposition of the energy terms indicated that both the attractive and repulsive terms are balanced. However, in total, the attractive terms dominate between the two molecular units, keeping the molecular units in the single material bound by weak forces. The electronic properties reveal the semiconductor nature in the bulk and surfaces, yet the band gap decreases upon downscaling from the bulk to the surface. The *I–V* characteristics show that slab-(001) of P_4Se_3 exhibits non-linear as well as applied gate-voltage dependent transport properties, behaving as FETs having complex transport properties, which can include resonance or many other quantum impacts specifically at higher applied gate voltages. The transmission spectra give useful insights regarding the energy-dependent nature of the electronic transport in the material. The presence of energy gaps and the resonant peaks in the transmission spectra has an impact on the shape of the *I–V* curves.

Conflicts of interest

The authors declare that they have no known competing financial interests or personal relationships that could have appeared to influence the work reported in this paper.

Data availability

The code for the Vienna *Ab initio* Simulation Package (VASP) can be found at **https://vaspkit.com/**, and Amsterdam density functional (ADF) can be found at **https://www.scm.com/**.[63]

Supplementary information is available: Frequency (THz) for the computed phonon modes. See DOI: **https://doi.org/10.1039/d5ra04194e**.

Acknowledgements

During the preparation of this work the author(s) used Gemini in order to improve the writing style. After using this tool/service, the author(s) reviewed and edited the content as needed and take(s) full responsibility for the content of the publication.

References

1 D. Xue, K. Li, J. Liu, C. Sun and K. Chen, Crystallization and functionality of inorganic materials, *Mater. Res. Bull.*, 2012, **47**(10), 2838–2842.
2 J. Uchida, B. Soberats, M. Gupta and T. Kato, Advanced functional liquid crystals, *Adv. Mater.*, 2022, **34**(23), 2109063.
3 W. Han, P. Huang, L. Li, F. Wang, P. Luo, K. Liu and T. Zhai, Two-dimensional inorganic molecular crystals, *Nat. Commun.*, 2019, **10**(1), 4728.
4 D. Wines, J. A. Kropp, G. Chaney, F. Ersan and C. Ataca, Electronic properties of bare and functionalized two-dimensional (2D) tellurene structures, *Phys. Chem. Chem. Phys.*, 2020, **22**(12), 6727–6737.
5 K. Liu, L. Liu and T. Zhai, Emerging two-dimensional inorganic molecular crystals: the concept and beyond, *J. Phys. Chem. Lett.*, 2022, **13**(9), 2173–2179.
6 X. Feng, X. Peng, B. Peng, Z. Li, W. Huang, S. Yang and T. Zhai, Effect of strong intermolecular interaction in 2D inorganic molecular crystals, *J. Am. Chem. Soc.*, 2021, **143**(48), 20192–20201.
7 A. Jabeen, A. Majid, M. Alkhedher, S. Haider and M. S. Akhtar, Impacts of structural downscaling of inorganic molecular crystals-A DFT study of Sb2O3, *Mater. Sci. Semicond. Process.*, 2023, **166**, 107729.

8 N. Z. Raza, A. Majid, A. Jabeen, S. Haider and K. Alam, First principles study on interactions in inorganic molecular crystals at zero dimensions, *J. Mol. Struct.*, 2024, **1317**, 139102.
9 B. Jin, F. Liang, Z. Y. Hu, P. Wei, K. Liu, X. Hu and T. Zhai, Nonlayered CdSe flakes homojunctions, *Adv. Funct. Mater.*, 2020, **30**(11), 1908902.
10 M. Kamiya, T. Tsuneda and K. Hirao, A density functional study of van der Waals interactions, *J. Chem. Phys.*, 2002, **117**(13), 6010–6015.
11 P. Kolandaivel, D. U. Maheswari and L. Senthilkumar, The study of performance of DFT functional for van der Waals interactions, *Comput. Theor. Chem.*, 2013, **1004**, 56–60.
12 H. W. Wang and M. Hayashi, A density functional theory study of van der Waals interaction in carbon nanotubes, *J. Chin. Chem. Soc.*, 2023, **70**(3), 759–769.
13 J. Hermann, R. A. DiStasio Jr and A. Tkatchenko, First-principles models for van der Waals interactions in molecules and materials: concepts, theory, and applications, *Chem. Rev.*, 2017, **117**(6), 4714–4758.
14 C. Tantardini, A. A. Michalchuk, A. Samtsevich, C. Rota and A. G. Kvashnin, The volumetric source function: looking inside van der Waals Interactions, *Sci. Rep.*, 2020, **10**(1), 7816.
15 W. Hu and J. Yang, Two-dimensional van der Waals heterojunctions for functional materials and devices, *J. Mater. Chem. C*, 2017, **5**(47), 12289–12297.
16 Y. Z. Abdullahi, R. Caglayan, A. Mogulkoc, Y. Mogulkoc and F. Ersan, New stable ultrawide bandgap As2O3 semiconductor materials, *J. Phys.: Mater.*, 2023, **6**(2), 025003.
17 A. Majid, A. Jabeen, S. U. D. Khan and Z. Almutairi, On the prospects of layeredness in tantalum pentoxide, *Mater. Sci. Eng., B*, 2021, **272**, 115349.
18 A. Majid and A. Jabeen, *Layeredness in Materials: Characteristics, Strategies and Applications*, Springer Nature, 2023.
19 A. Majid and A. Jabeen, *Layeredness in Materials: Characteristics, Strategies and Applications*, Springer Nature, 2023.
20 A. Majid and A. Jabeen, Characteristics, Strategies and Applications of Layered Materials: An Introduction, in *Layeredness in Materials: Characteristics, Strategies and Applications*, Springer Nature Singapore, Singapore, 2023, pp. 1–16.
21 G. M. Mustafa, N. A. Noor, M. W. Iqbal, M. Sajjad, M. A. Naeem, Q. Mahmood and W. Al-Masry, Study of optoelectronic and transport properties of MgLu2Z4 (Z = S, Se) spinels for optoelectronic and energy harvesting applications, *Mater. Sci. Semicond. Process.*, 2021, **121**, 105452.
22 D. H. Ozbey, M. E. Kilic and E. Durgun, Promising anisotropic mechanical, electronic, and charge transport properties of 2D InN alloys for photocatalytic water splitting, *Appl. Surf. Sci.*, 2023, **638**, 157982.
23 K. Liu, B. Jin, W. Han, X. Chen, P. Gong, L. Huang and T. Zhai, A wafer-scale van der Waals dielectric made from an inorganic molecular crystal film, *Nat. Electron.*, 2021, **4**(12), 906–913.
24 Y. Zhang, Inorganic molecular crystal dielectric film enabling high-performance 2D van der Waals devices and scalable integration, *Sci. Bull.*, 2022, **67**(10), 1010–1012.
25 R. Blachnik, The compounds P4S3, P4Se3, As4S3 and As4Se3 and the quaternary system P4S3-P4Se3-As4S3-As4Se3, *Thermochim. Acta*, 1993, **213**, 241–259.
26 M. Gardner, Infrared and Rman spectra of some phosphorus sulphides, *J. Chem. Soc., Dalton Trans.*, 1973, (6), 691–696.
27 J. R. Rollo, G. R. Burns, W. T. Robinson, R. J. Clark, H. M. Dawes and M. B. Hursthouse, A new polymorph of tetraphosphorus triselenide,. alpha.'-P4Se3: an x-ray, Raman, and XPS study of the normal crystalline phases and a DSC study of the crystalline and the orientationally disordered phases of P4Se3, *Inorg. Chem.*, 1990, **29**(16), 2889–2894.
28 R. Blachnik and U. Wickel, Thermal behaviour of A4B3 cage molecules (A = P, As; B = S, Se), *Thermochim. Acta*, 1984, **81**, 185–196.
29 A. M Majid, N. Z. Raza, S. Haider, K. Alam and S. Naeem, Electronic Transport Properties of Molecular Clusters Sb4O6, P4Se3, and P4O6, *J. Phys. Chem. A*, 2024, **128**(24), 4814–4822.
30 Y. Tan, L. Chen, H. Chen, Q. Hou and X. Chen, Synthesis of a symmetric bundle-shaped Sb2O3 and its application for anode materials in lithium ion batteries, *Mater. Lett.*, 2018, **212**, 103–106.
31 Y. Cao, M. K. Majeed, Y. Li, G. Ma, Z. Feng, X. Ma and W. Ma, P4Se3 as a new anode material for sodium-ion batteries, *J. Alloys Compd.*, 2019, **775**, 1286–1292.
32 A. Majid, N. Z. Raza, S. Ahmad and M. Alkhedher, Electrochemical performance of P4Se3 as high-capacity anode materials for monovalent and multivalent ion batteries, *Mater. Chem. Phys.*, 2024, **322**, 129515.
33 Y. Ou, X. Li, J. Kopaczek, A. Davis, G. Jackson, M. Sayyad and S. A. Tongay, The Hard Ferromagnetism in FePS3 Induced by Non-Magnetic Molecular Intercalation, *Adv. Phys. Res.*, 2025, **4**(2), 2400101.
34 A. Kubaib, P. M. Imran and A. A. Basha, Applications of the Vienna Ab initio simulation package, DFT and molecular interaction studies for investigating the electrochemical stability and solvation performance of non-aqueous NaMF6 electrolytes for sodium-ion batteries, *Comput. Theor. Chem.*, 2022, **1217**, 113934.
35 L. Rodriguez, Ab initio computational modeling of surface supercells of pseudo-cubic halide perovskites, Doctoral dissertation, Texas State University, 2023.
36 M. F. Chen, Y. Chen, Z. J. Lim and M. W. Wong, Adsorption of imidazolium-based ionic liquids on the Fe (1 0 0) surface for corrosion inhibition: physisorption or chemisorption?, *J. Mol. Liq.*, 2022, **367**, 120489.
37 X. Wang, A. Hobhaydar, Y. Wang, D. Wexler, H. Li, N. V. Tran and H. Zhu, Unveiling the oxidation mechanism of CrTaTiMo refractory medium-entropy alloys: a synergy of density functional theory and ab initio molecular dynamics, *Mater. Des.*, 2024, **240**, 112832.

38 W. S. Morgan, J. E. Christensen, P. K. Hamilton, J. J. Jorgensen, B. J. Campbell, G. L. Hart and R. W. Forcade, Generalized regular k-point grid generation on the fly, *Comput. Mater. Sci.*, 2020, **173**, 109340.

39 A. Majid, T. M. Younes, A. Jabeen, H. Batool, M. Alkhedher and S. M. ElDin, Predictions on Structural and Electronic Properties to Synthesize Bismuth-Carbon Compounds in Different Periodicities, *Materials*, 2022, **15**(22), 8150.

40 A. Majid, A. Jabeen and M. Farooq, First Principles Investigation to Explore Effects of Thulium Doping on Electronic Properties of ZnO, *Pak. J. Sci. Ind. Res., Ser. A*, 2025, **68**(1), 8–14.

41 T. Märkl, S. Salehitaleghani, M. Le Ster, P. J. Kowalczyk, X. Wang, P. Wang and S. A. Brown, Antimony oxide nanostructures in the monolayer limit: self-assembly of van der Waals-bonded molecular building blocks, *Nanotechnology*, 2020, **32**(12), 125701.

42 Y. Xu, S. Zhang, W. Wu and P. Su, Assessments of DFT-based energy decomposition analysis methods for intermolecular interactions, *J. Chem. Phys.*, 2023, **158**(12), 124116.

43 Z. Tang, B. Shao, W. Wu and P. Su, Energy decomposition analysis methods for intermolecular interactions with excited states, *Phys. Chem. Chem. Phys.*, 2023, **25**(27), 18139–18148.

44 L. Zhao, M. Hermann, W. E. Schwarz and G. Frenking, The Lewis electron-pair bonding model: modern energy decomposition analysis, *Nat. Rev. Chem.*, 2019, **3**(1), 48–63.

45 P. T. Mathew and F. Fang, Periodic energy decomposition analysis for electronic transport studies as a tool for atomic scale device manufacturing, *Int. J. Extreme Manuf.*, 2020, **2**(1), 015401.

46 A. D. Wonanke and M. A. Addicoat, Effect of unwanted guest molecules on the stacking configuration of covalent organic frameworks: a periodic energy decomposition analysis, *Phys. Chem. Chem. Phys.*, 2022, **24**(25), 15494–15501.

47 T. S. Amer, F. M. El-Sabaa, G. M. Moatimid, S. K. Zakria and A. A. Galal, On the stability of a 3DOF vibrating system close to resonances, *J. Vib. Eng. Technol.*, 2024, **12**(4), 6297–6319.

48 A. M. Abdullahi, Z. Mohamed, M. Z. Abidin, R. Akmeliawati and A. A. Bature, Stability analysis and vibration control of a class of negative imaginary systems, *J. Teknol. Lab.*, 2015, **77**(17), 12.

49 M. Esters, C. Oses, D. Hicks, M. J. Mehl, M. Jahnátek, M. D. Hossain and S. Curtarolo, Settling the matter of the role of vibrations in the stability of high-entropy carbides, *Nat. Commun.*, 2021, **12**(1), 5747.

50 F. L. Thiemann, P. Rowe, E. A. Muller and A. Michaelides, Machine learning potential for hexagonal boron nitride applied to thermally and mechanically induced rippling, *J. Phys. Chem. C*, 2020, **124**(40), 22278–22290.

51 X. Yu, H. Shao, X. Wang, Y. Zhu, D. Fang and J. Hong, Anomalous lattice thermal conductivity in layered MNCl (M = Zr, Hf) materials driven by lanthanide contraction, *J. Mater. Chem. A*, 2020, **8**(6), 3128–3134.

52 M. Azmat, A. Majid, M. Alkhedher, S. Haider and M. S. Akhtar, A first-principles study on two-dimensional tetragonal samarium nitride as a novel photocatalyst for hydrogen production, *Int. J. Hydrogen Energy*, 2023, **48**(79), 30732–30740.

53 M. H. Lakhdar, Y. B. Smida and M. Amlouk, Synthesis, optical characterization and DFT calculations of electronic structure of Sb2O3 films obtained by thermal oxidation of Sb2S3, *J. Alloys Compd.*, 2016, **681**, 197–204.

54 B. G. Janesko, Replacing hybrid density functional theory: motivation and recent advances, *Chem. Soc. Rev.*, 2021, **50**(15), 8470–8495.

55 R. Shinde, S. S. Yamijala and B. M. Wong, Improved band gaps and structural properties from Wannier–Fermi–Löwdin self-interaction corrections for periodic systems, *J. Phys.: Condens. Matter*, 2020, **33**(11), 115501.

56 R. Shinde, S. S. Yamijala and B. M. Wong, Improved band gaps and structural properties from Wannier–Fermi–Löwdin self-interaction corrections for periodic systems, *J. Phys.: Condens. Matter*, 2020, **33**(11), 115501.

57 S. Soni, G. Ye, J. Zheng, Y. Zhang, A. Asyuda, M. Zharnikov and R. C. Chiechi, Understanding the Role of Parallel Pathways via In-Situ Switching of Quantum Interference in Molecular Tunneling Junctions, *Angew. Chem., Int. Ed.*, 2020, **59**(34), 14308–14312.

58 Y. Mao and Z. Huang, Electron transport properties of van der Waals heterostructures composed by one-dimensional carbon nanotubes and two-dimensional germanium selenide, *Results Phys.*, 2023, **52**, 106835.

59 H. Batool, A. Majid, M. Alkhedher, N. Bulut and I. Al-Adwan, A DFT study of quantum electronic transport properties of InTeCl, *Mater. Sci. Semicond. Process.*, 2023, **168**, 107842.

60 S. Choudhary and S. Qureshi, Effect of radial and axial deformation on electron transport properties in a semiconducting Si-C nanotube, *J. Nano- Electron. Phys.*, 2011, **3**(1), 584.

61 S. Datta, *Quantum Transport: Atom to Transistor*, Cambridge University Press, 2005.

62 Z. Li and D. S. Kosov, Dithiocarbamate anchoring in molecular wire junctions: a first principles study, *J. Phys. Chem. B*, 2006, **110**(20), 9893–9898.

63 J. Hafner, Ab-initio simulations of materials using VASP: density-functional theory and beyond, *J. Comput. Chem.*, 2008, **29**(13), 2044–2078.